Discover Nano

RESEARCH Open Access

Computational study to heat and mass transfer analysis of blood-based Maxwell ternary hybrid nanofluid with nonlinear thermal radiation and exponential heat source

Ibrahim Mahariq[1,2,3,4], Syed Arshad Abas[5], Mehreen Fiza[5], Hakeem Ullah[5*], Ali Akgül[6,7,8,9], Mukhlisa Soliyeva[10], Hasan AKSOY[11] and Seham M. Al-Mekhlafi[12*]

*Correspondence:
Hakeem Ullah
hakeemullah1@gmail.com
Seham M. Al-Mekhlafi
sehammalmekhlafi@gmail.com

Full list of author information is available at the end of the article

Abstract

This study presents a ternary hybrid nanofluid model exhibiting superior thermal performance as compared to conventional fluids. The ternary hybrid nanofluid is formulated by suspending alumina Al_2O_3, silicon dioxide (SiO_2), and Titanium dioxide (TiO_2) nanoparticles in blood, and its flow is model using non-Newtonian Maxwell model. Furthermore, the combined effects of nonlinear thermal radiation and space-based heat source are incorporated. The system of ordinary differential equations (ODEs), which is obtained via the use of similarity transformations, is solved numerically by the bvp4c technique in MATLAB. The impact of different physical parameters are displayed through Figures and Tables. Results show that amplifying the magnetic field, porosity, and Maxwell parameters diminishes the velocity of ternary and hybrid nanofluid. The skin friction enhances 10% and 3.1% for magnetic parameter and Maxwell fluid parameter respectively. The elevated numbers of radiation, space-dependent heat source and thermal Biot number amplify the temperature distribution. Nusselt number of ternary hybrid nanofluid improves 2.3% for thermal radiation, 1% for heat source, 1.2% for temperature difference parameter and 3% for Biot number.

Keywords Stretching surface, Ternary hybrid nanofluid, Space-based heat source, Joule heating, bvp4c

1 Introduction

Nanofluids are sophisticated fluids formed by the incorporation of nanoparticles, which are minuscule particles at the nanometer size, into a base fluid such as water, oil, or ethylene glycol. These nanoparticles, composed of metals (e.g., copper or silver), metal oxides (e.g., aluminium oxide or titanium dioxide), or carbon-based materials (e.g., carbon nanotubes or graphene), markedly enhance the thermal conductivity and heat transfer efficiency of the base fluid. This breakthrough enhances performance across

© The Author(s) 2026. **Open Access** This article is licensed under a Creative Commons Attribution-NonCommercial-NoDerivatives 4.0 International License, which permits any non-commercial use, sharing, distribution and reproduction in any medium or format, as long as you give appropriate credit to the original author(s) and the source, provide a link to the Creative Commons licence, and indicate if you modified the licensed material. You do not have permission under this licence to share adapted material derived from this article or parts of it. The images or other third party material in this article are included in the article's Creative Commons licence, unless indicated otherwise in a credit line to the material. If material is not included in the article's Creative Commons licence and your intended use is not permitted by statutory regulation or exceeds the permitted use, you will need to obtain permission directly from the copyright holder. To view a copy of this licence, visit http://creativecommons.org/licenses/by-nc-nd/4.0/.

various applications, including cooling systems, energy systems, and medical technologies. Droplet trains cooling technology is used for increasing thermal management in high heat flux electronic devices [1]. Nanofluids comprising two varieties of nanoparticles are referred to as hybrid nanofluids. This hybridization leverages the augmentative characteristics of each nanoparticle type. Moghimi et al. [2] numerically studied the nanofluid flow and found that temperature was enhanced by 540%, with Hartmann number. The viscoelastic parameter influences the nanofluid velocity, by creating greater resistance [3]. Fu et al. [4] theoretical study the application of the nanofluid in oil recovery. Razzaq et al. [5] analyzed hybrid nanofluid flow with viscous and Joule dissipation. It was examined that increasing the stretching parameter leads to an escalation in the momentum profile. Panda et al. [6] focused at the role of Cattneo-Christov heat flux model and thermal radiation in hybrid nanofluid flow. A nacre-inspired hybrid nanofluid composite, as reported by Hu et al. [7] delivers high passive radiative cooling power with enhanced energy and reduce carbon emissions. Mahmood et al. [8] deliberated the viscous dissipative hybrid nanofluid flow with MHD effects. Yasir et al. [9] studied the hybrid nanofluid flow over a shrinking surface and found that thermal profiles enhances with heat source. Urooj et al. [10] examined the thermal radiation effect on hybrid nanofluid flow using the Cattaneo-Christov heat flux model. A surface area engineered MWCNT + Al_2O_3 hybrid nanocomposite, reported by Ai et al. [11] enhance combustion and thermal efficiency. Hybrid nanofluid containing Au and SiO_2 nanoparticles has significant application in cooling and thermal management system [12]. Abas et al. [13] discussed the hybrid nanofluid flow containing copper and silver nanoparticles past between revolving disks. They found that growth in magnetic parameter decreases the speed of the nanoparticles. A hybrid fluid flow coupled with Cattaneo-Christov model, a complex heat transfer phenomenon with significant implification for industrial and engineering applications [14]. Ternary hybrid nanofluids represent an advanced iteration of this concept, incorporating the dispersion of three distinct types of nanoparticles in the base fluid. This technology allows significant customization of the fluid's properties by integrating the unique advantages of each type of nanoparticle. Gangadhar and Dinarvand [15] examined a comparative analysis of nano, hybrid and ternary hybrid nanofluid having nanoparticles Cu, Ag and CuO and deduced that heat transfer rate in more effective in ternary hybrid nanofluid. Heat transfer rate enhanced by 8.7% for ternary hybrid nanofluid as compared to other fluids [16]. Varatharaj et al. [17] used three distinct sorts of nanoparticles, including silver, titanium oxide and Alumina, to study ternary hybrid nanofluid flow past a permeable enlarging surface. The decreasing performance in the velocity distribution is noted for greater porosity parameter. Yasir et al. [18] explored the MHD ternary hybrid nanofluid buoyancy driven flow under the velocity slip and Melting boundary conditions. Thamizhselvi et al. [19] investigated the sodium alginate-based ternary hybrid nanofluid flow containing MgO, MoS2 and SWCNT over an exponential stretching porous surface. The addition of nanoparticles in base fluid improved the thermal panel of the ternary hybrid nanofluid flow [20]. Yasir et al. [21] analyzed the heat source effect of MHD flow of alumina and silica/Methanol hybrid nanofluid Moltot et al.[22] discussed the role of variable thermal conductivity and nonlinear thermal radiation on ethylene glycol-based ternary hybrid nanofluid containing silver, copper, and alumina nanoparticles over a stretching surface. A comparative analysis made by Mahboobtosi et al. [23] to inspect the ternary hybrid nanofluid flow. Ternary hybrid

nanofluids have a lot of potential for a wide range in oil recovery and Biomedical therapies [24] and technical and industrial uses that call for effective heat control due to their flexibility [25–27].

An exponential space-based heat source exhibiting shear-thinning/thickening behavior provides novel perspectives for optimizing thermal transport processes in intricate systems, including the cooling of microelectronics, energy storage technologies, and biomedical devices, where precise thermal regulation is essential. Shah et al. [28] inspected the impact of an exponential space-based heat source for Carreau water-based ternary hybrid nanofluid flow and found that the thermal profile significantly improved for ternary hybrid nanofluid. Khan et al. [29] examined the impacts of nonlinear thermal radiation as well as an exponential space-based heat source on ternary hybrid nanofluid flow over a stretching surface. Shamshuddin et al. [30] used Homotopy analysis method to investigate the Non-Newtonian micropolar flow with heat generation and slip effects. Lone et al. [31] examined an exponential space-based heat source in MHD ternary hybrid nanofluid flow with slip effects. The existence of heat source and sink increases the temperature of the ternary hybrid nanofluid by altering heat generation [32]. Shamshuddin et al. [33] examined the consequences of heat source and thermal radiation on MHD ternary hybrid nanofluid. Sarfraz and Muhammad [34] investigated the MHD flow with the inclusion of heat source using Keller-Box method. Their consequences showed that the skin friction coefficient has augmented with expansion in magnetic and porosity factors. Bilal and Yasir [35] conceded the formulation representing thermophysical relation for ternary hybrid nanofluid past a stretching and shrinking surface with variable heat source.

Joule heating, also known as Ohmic heating, is the phenomenon in which electrical energy is converted into thermal energy as an electric current crosses a conductor. This effect plays a pivotal role in numerous applications, including magnetic refrigeration and electronic cooling, where it can substantially impact thermal regulation and energy efficiency. Takreem et al. [36] examined the heat transfer of magnetohydrodynamic ternary hybrid nanofluid flow with Joule heating. It was perceived that heat transfer rate is more pronounced for ternary hybrid nanofluid. Hussain et al. [37] scrutinized the ternary hybrid nanofluid flow with Joule heating, showing that higher suction parameter boosts the heat transfer rate by 1%. Naveed et al. [38] inspected the outcome of Joule heating and melting conditions on a hybrid nanofluid flow. Patel et al. [39] scrutinized the Joule heating and thermal radiation under slip condition. Mumtaz et al. [40] studied the thermal behavior of tetra hybrid nanofluid with Joule heating. Ramesh et al. [41] numerically investigated the slip flow over a stretching surface incorporating the effect of Joule heating and thermal radiation. According to Yasir and Khan [42], the Joule heating phenomenon is used to raise the temperature of the hybrid nanofluid. Rasheed et al. [43] investigated the effects of chemically reactive and Joule heating effects on MHD flow. The outcomes show that as magnetic parameter grows, the velocity distribution drops, while the thermal panel boosts.

The study of the fluid over an extended sheet holds significant industrial and engineering applications, particularly in polymer manufacturing and electrochemistry. In flow dynamics, stretching sheet models are also applicable to processes such formation of paper and glass production. A stretching sheet hybrid nanofluid flow was modeled by Riaz et al. [44] using Williamson fluid model. Waqas et al. [45] deliberated the thermally

radiative hybrid nanofluid flow past an enlarging surface and found that the velocity profile declines with the increasing magnetic factor. Ziabakhsh et al. [46] probed to create a chemically affected, and analytically solvable diffusion-type flow in which fluids may move through a stretch sheet used in cutting-edge engineering and manufacturing. Kausar et al. [47] numerically addressed the mixed convective flow over an extending surface. Their finding reveals that velocity panel diminished with growth in porosity factor. The collective impacts of heat source and magnetohydrodynamic on a hybrid nanofluid flow across a dual directional stretching surface studied by Zangooee et al. [48]. The convective and zero mass flux effects were studied by Abas et al. [49] to examine the blood-based flow past a stretching sheet. The rate of the heat transmission over an exponential stretching surface studied by Zainal et al. [50].

According to the reviewed literature, numerous studies have investigated hybrid nanofluid flow over a stretching surface. However, limited number addressed MHD ternary hybrid nanofluid Maxwell flow in heat and mass transfer mechanism over a stretching surface.

The following gaps are addressed:

1. The rheology of non-Newtonian Maxwell model is studied over a stretching porous surface.
2. Three sorts of nanoparticles Al_2O_3, TiO_2 and SiO_2 are suspended in Blood serve as base fluid.
3. Exponential heat source and non-linear thermal radiation are addressed.
4. Thermal and mass convective condition are incorporated at the surface of the sheet for the characterization of heat and mass transfer.
5. A numerical technique bvp4c is utilized for complex model.

1.1 Objectives

The objectives of the current study are:

1. To examine the effect of ternary nanoparticles on different flow profiles.
2. To investigate how nanoparticles (hybrid and ternary) influence the skin friction, heat and mass transfer rate.
3. In this analysis examine the effect of thermal and mass convective boundary conditions on the ternary hybrid nanofluid flow over a stretching surface.
4. In this analysis the exponential heat source is considered.
5. To examine the effect of thermal radiation and viscous dissipation on hybrid and ternary hybrid nanofluid.

1.2 Research questions

The significant research questions arise regarding this study are:

1. Which nanofluids (hybrid or ternary hybrid) have more influenced the non-Newtonian Maxwell flow?
2. How the heat source and nonlinear thermal radiation effects the thermal performance?
3. How the Maxwell parameter effects the velocity of hybrid and ternary hybrid nanofluids?
4. Which type of nanolfuids has a higher skin friction, heat and mass transfer rate under increasing values of used physical factors?

2 Problem description

This section addresses steady, two-dimensional, incompressible ternary hybrid Maxwell nanofluid flow over a stretching porous surface. The ternary hybrid nanofluid is composed of (Al_2O_3), (TiO_2) and (SiO_2) nanoparticles dispersed in blood which serve as base fluid. The nanoparticles are assumed to be uniformly dispersed, spherical in shape, and in thermal equilibrium with the base fluid. Agglomeration, sedimentation, and slip between the nanoparticles and the base fluid are neglected. The thermophysical properties are assumed to be constant. The velocity components u and v aligned along $x-$ and $y-$ axes, respectively. The flow is induced by the stretching of the porous sheet in the $x-$ direction with stretching velocity $u_w = ax$. A magnetic field of intensity B_0 is applied transversely to the flow direction. The induced magnetic field is neglected, which is justified by the assumption of a low magnetic Reynolds number. A schematic illustration of the flow configuration is sketched in Fig. 1. A hot fluid with reference temperature T_F and heat transfer coefficient h_F convects heat towards the sheet surface. The temperature and concentration of the surface is $T_w(T_w < T_F)$ and C_w respectively. The free stream temperature and concentration are denoted by T_∞ and C_∞. Furthermore, the effect of nonlinear thermal radiation, exponential heat source, and chemical reaction is incorporated into the model. Thermal and, mass convective conditions are applied at the sheet surface. Based on the above assumptions, the leading equations are expressed as follows [51–53].

2.1 Continuity equation

$$\frac{\partial u}{\partial x} + \frac{\partial u}{\partial y} = 0 \tag{1}$$

Here, $(x-)$ and $(y-)$ are coordinate axis along with their respective velocity u $(x-)$ and $v(y-)$.

2.2 Momentum equation

$$u\frac{\partial u}{\partial x} + v\frac{\partial u}{\partial y} = \frac{\mu_{Thnf}}{\rho_{Thnf}}\frac{\partial^2 u}{\partial y^2} - \frac{\sigma_{Thnf}}{\rho_{Thnf}}B_0^2 u - \frac{\mu_{Thnf}}{\rho_{Thnf}k^*} - \frac{\lambda}{\rho_{Thnf}}\left(u^2\frac{\partial^2 u}{\partial x^2} + v^2\frac{\partial^2 v}{\partial y^2} + 2uv\frac{\partial^2 u}{\partial y \partial x}\right) \tag{2}$$

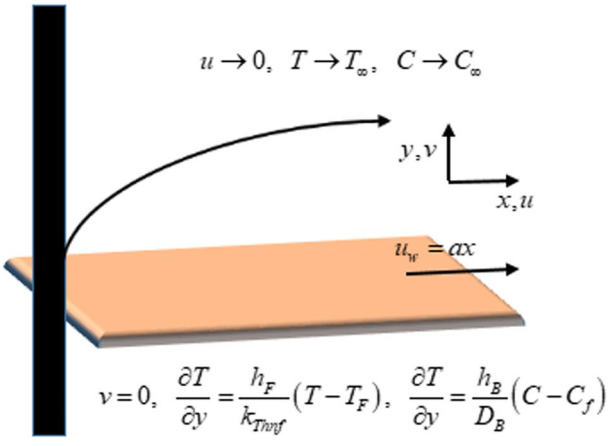


Fig. 1 Geometry of the model

In the above Eq. (2), B_0 is the magnetic field strength, μ_{Thnf} and ρ_{Thnf} is the dynamic viscosity and density of the ternary hybrid nanofluid, λ is the Maxwell parameter.

2.3 Energy equation

$$\begin{aligned} u\frac{\partial T}{\partial x}+v\frac{\partial T}{\partial y}=\frac{k_{Thnf}}{(\rho C_p)_{Thnf}}\frac{\partial^2 T}{\partial y^2}+\frac{(\rho C_p)_{np}}{(\rho C_p)_{Thnf}}\left[D_B\frac{\partial C}{\partial y}\frac{\partial T}{\partial y}+\frac{D_T}{T_\infty}\left(\frac{\partial T}{\partial y}\right)^2\right]+\frac{\sigma_{Thnf}}{(\rho C_p)_{Thnf}}B_0^2u^2 \\ -\frac{1}{(\rho C_p)_{Thnf}}\frac{\partial q_r}{\partial y}+\frac{\mu_{Thnf}}{(\rho C_p)_{Thnf}}\left(\frac{\partial u}{\partial y}\right)^2+\frac{Q_s}{(\rho C_p)_{Thnf}}\left(T_F-T_\infty\right)Exp\left(-ny\sqrt{\frac{a}{\vartheta_F}}\right), \end{aligned} \tag{3}$$

Here T is the temperature of the fluid, D_B is the thermophoresis diffusion coefficient, Q_e heat source factor, k_{Thnf} is thermal conductivity $(\rho C_p)_{Thnf}$ is heat capacitance and σ_{Thnf} electrical conductivity of the ternary hybrid nanofluid. q_r is the radiative heat flux, which is defined as [54]:

$$q_r=\frac{4\sigma_e}{3k_e}\left(3T^2\left(\frac{\partial T}{\partial y}\right)^2+T^3\frac{\partial^2 T}{\partial y^2}\right) \tag{4}$$

2.4 Concentration equation

$$\left(u\frac{\partial}{\partial x}+v\frac{\partial}{\partial y}\right)C=D_B\frac{\partial}{\partial y}\left(\frac{\partial C}{\partial y}+\frac{D_T}{T_\infty}\frac{\partial T}{\partial y}\right)-K_a\left(C-C_\infty\right), \tag{5}$$

In this equation C is the concentration of the fluid, D_B is the Brownian diffusion coefficient and K_a is reaction rate parameter.

Subject to the below boundary constraints [55, 56];

$$\left.\begin{array}{l} u\left(y\to\infty\right)=u_{wx}\left(x\right),\ \ v=0,\ \ \dfrac{\partial T\left(y\to\infty\right)}{\partial y}=\dfrac{h_F}{k_{Thnf}}\left(T-T_F\right), \\ \dfrac{\partial C\left(y\to\infty\right)}{\partial y}=\dfrac{h_B}{D_B}\left(C-C_F\right), \\ u\left(y\to\infty\right)\to 0,\ C\left(y\to\infty\right)\to C_\infty\ T\left(y\to\infty\right)\to T_\infty \end{array}\right\}, \tag{6}$$

In the boundary conditions, u_w is stretching velocity, h_F heat transfer coefficient, h_B is the mass transfer coefficient, T_F and C_F are reference temperature and concentration while at far field is T_∞ and C_∞.

In Table 1, the thermophysical properties of the ternary and hybrid nanofluids are labeled. Moreover, the nanoparticle volume fraction is denoted by $(=\varphi)$, where, the subscript $(s1)$ is first nanoparticle, $(s2)$ is second nanoparticle and $(s3)$ represent third nanoparticle.

The numerical values of the nanoparticle as base fluid is shown in Table 2.

The set of suitable similarity variables is [55]:

$$\left.\begin{array}{l} \eta=\left(\dfrac{a}{\vartheta_F}\right)^{1/2}y,\ u=axF'\left(\eta\right),T-T_\infty=\left(T_F-T_\infty\right)\theta\left(\eta\right), \\ C-C_\infty=\left(C_F-C_\infty\right)\phi\left(\eta\right),v=-\left(a\vartheta_F\right)^{1/2}F\left(\eta\right) \end{array}\right\} \tag{7}$$

After utilizing Eq. (7) in Eqs. (1–6), the following non-dimensional form is obtained.

Table 1 The thermophysical properties are defined as [37]

Dynamic viscosity	$\mu_{hnf} = \frac{\mu_F}{\sqrt{(1-\varphi_{s1})(1-\varphi_{s2})}}$,
	$\mu_{Thnf} = \frac{\mu_F}{\sqrt{(1-\varphi_{s1})(1-\varphi_{s2})(1-\varphi_{s3})}}$
Heat capacitance	$(\rho C_p)_{hnf} = (1-\varphi_{s2})\left[\left\{(1-\varphi_{s1})(\rho C_p)_F + \varphi_{s1}(\rho C_p)_{s1}\right\}\right] + \varphi_{s2}(\rho C_p)_{s2}$
	$(\rho C_p)_{Thnf} = (1-\varphi_{s3})\begin{bmatrix}(1-\varphi_{s2})\left\{(1-\varphi_{s1})(\rho C_p)_F + \varphi_{s1}(\rho C_p)_{s1}\right\}\\ +\varphi_{s2}(\rho C_p)_{s2}\end{bmatrix} + \varphi_{s3}(\rho C_p)_{s3}$
Density	$\rho_{hnf} = (1-\varphi_{s2})[\{(1-\varphi_{s1})\rho_F + \varphi_{s1}\rho_{s1}\}] + \varphi_{s2}\rho_{s2}$
	$\rho_{Thnf} = (1-\varphi_{s3})[(1-\varphi_{s2})\{(1-\varphi_{s1})\rho_F + \varphi_{s1}\rho_{s1}\} + \varphi_{s2}\rho_{s2}] + \varphi_{s3}\rho_{s3}$
Electrical conductivity	$\frac{\sigma_{Thnf}}{\sigma_{hnf}} = \frac{(1+2\varphi_{s3})\sigma_{s3} + 2(1-\varphi_{s3})\sigma_{hnf}}{(\sigma_{s3}-\sigma_{s3}\varphi_{s3}) + \left(2\sigma_{hnf}+\sigma_{hnf}\varphi_{s3}\right)}, \frac{\sigma_{nf}}{\sigma_F} = \frac{(1+2\varphi_{s1})\sigma_{s1} + 2(\sigma_F - \sigma_F\varphi_{s1})}{(\sigma_{s1}-\sigma_{s1}\varphi_{s1}) + (2\sigma_F+\sigma_F\varphi_{s1})},$
	$\frac{\sigma_{hnf}}{\sigma_{nf}} = \frac{(1+2\varphi_{s2})\sigma_{s2} + 2(1-\varphi_{s2})\sigma_{nf}}{(\sigma_{s2}-\sigma_{s2}\varphi_{s2}) + \left(2\sigma_{nf}+\sigma_{nf}\varphi_{s2}\right)}$
Thermal conductivity	$\frac{k_{Thnf}}{k_{hnf}} = \frac{(1+2\varphi_{s3})k_{s3} + 2(1-\varphi_{s3})k_{hnf}}{(k_{s3}-k_{s3}\varphi_{s3}) + \left(2k_{hnf}+k_{hnf}\varphi_{s3}\right)}, \frac{k_{hnf}}{k_{nf}} = \frac{(1+2\varphi_{s2})k_{s2} + 2(1-\varphi_{s2})k_{nf}}{(k_{s2}-k_{s2}\varphi_{s2}) + \left(2k_{nf}+k_{nf}\varphi_{s2}\right)},$
	$\frac{k_{nf}}{k_F} = \frac{(1+2\varphi_{s1})k_{s1} + 2(k_F - k_F\varphi_{s1})}{(k_{s1}-k_{s1}\varphi_{s1}) + (2k_F+k_F\varphi_{s1})},$

$$\frac{\mu_{Thnf}}{\mu_f}F''' - \frac{\rho_{Thnf}}{\rho_f}\left(F'^2 + FF''\right) - \frac{\sigma_{Thnf}}{\sigma_f}MF' - \frac{\mu_{Thnf}}{\mu_f}KpF' - \beta\left(F^2F''' - 2FF'F''\right) = 0, \tag{8}$$

$$\begin{aligned}&\frac{k_{Thnf}}{k_F}\theta'' + \left(Rd\left(\theta\left(\theta_w - 1\right) + 1\right)^2\left(3\theta'^2\left(\theta_w - 1\right) + \left(\theta\left(\theta_w - 1\right) + 1\right)\theta''\right)\right) + \frac{\sigma_{Thnf}}{\sigma_F}\Pr MEcF'^2,\\ &\frac{\left(\rho C_p\right)_{Thnf}}{\left(\rho C_p\right)_F}\Pr F\theta' + \Pr\left(Nb\theta'\phi' + Nt\theta'^2\right) + \frac{\mu_{Thnf}}{\mu_F}\Pr EcF''^2 + \Pr Q_a Exp\left(-n\eta\right) = 0\end{aligned} \tag{9}$$

$$Nb\phi'' + NbSc\left(F\phi' - \Omega\phi\right) + Nt\theta'' = 0, \tag{10}$$

$$\left.\begin{aligned}&F\left(\eta = 0\right) = 0,\ F'\left(\eta = 0\right) = 1,\ \frac{k_{Thnf}}{k_F}\theta'\left(\eta = 0\right) = -BiT\left(1 - \theta\left(\eta = 0\right)\right)\\ &\phi'\left(\eta = 0\right) = -Bc\left(1 - \phi\left(\eta = 0\right)\right)\\ &F'\left(\eta = \infty\right) = 0,\ \theta\left(\eta = \infty\right) = 0,\ \ \phi\left(\eta = \infty\right) = 0)\end{aligned}\right\} \tag{11}$$

The emerging parameters in dimensionless form are defined as follows:

Magnetic parameter is $M = \frac{\sigma_F B_0^2}{\rho_F a}$, Schmidt number is $Sc = \frac{\mu_F}{\rho_F D_B}$, Brownian motion parameter is $Nb = \frac{\left(\rho C_p\right)_{np} D_B\left(C_F - C_\infty\right)}{\left(\rho C_p\right)_F \vartheta_F}$, Concentration Biot number is $Bc = \frac{h_c}{k_F}\sqrt{\frac{\vartheta_F}{a}}$, Chemical reaction parameter is $\Omega = \frac{K_a}{a}$, Prandtl number is $\Pr = \frac{\left(\mu C_p\right)_F}{k_F}$, Eckert number is $Ec = \frac{u_w^2}{\left(C_p\right)_F\left(T_F - T_\infty\right)}$, Thermophoresis parameter is $Nt = \frac{\left(\rho C_p\right)_{np} D_T\left(T_F - T_\infty\right)}{\left(\rho C_p\right)_F \vartheta_F T_\infty}$, Biot number is $BiT = \frac{h_F}{k_F}\sqrt{\frac{\vartheta_F}{a}}$, porosity parameter is $Kp = \frac{\mu_F}{a\rho_F k^*}$, Temperature difference parameter is $\theta_w = \frac{T_F}{T_\infty}$, Radiation parameter is $Rd = \frac{16\sigma_e T_\infty^3}{3k_e k_F}$,Heat source $Q_a = \frac{Q_s}{a\left(\rho C_p\right)_F}$,and Maxwell parameter is $\beta = \frac{\lambda a}{\rho_F}$.

3 Quantity of interest

The engineering quantities like skin friction, Nusselt number and Sherwood number are defined as:

$$\left.\begin{aligned}C_{fx} &= \frac{\left(\mu_{Thnf}\frac{\partial u_x}{\partial y}\Big|_{y=0}\right)}{\rho_F\left(u_w\left(x\right)\right)^2},\\ Nu_x &= \frac{x\left(-k_{Thnf}\frac{\partial T}{\partial y}\Big|_{y=0}\right) + q_r|_{y=0}}{k_F\left(T_F - T_\infty\right)},\\ Sh_x &= \frac{x\left(-D_B\frac{\partial C}{\partial y}\Big|_{y=0}\right)}{D_B\left(C_F - C_\infty\right)}.\end{aligned}\right\} \tag{12}$$

After simplification the following reduce forms are obtained.

$$\left.\begin{aligned}SF_x &= C_{fx}\sqrt{\mathrm{Re}_x} = \frac{\mu_{Thnf}}{\mu_F}F''\left(0\right),\ Sw = \frac{Sh_x}{\sqrt{\mathrm{Re}_x}} = -\phi'\left(0\right)\\ Ns &= \frac{Nu_x}{\sqrt{\mathrm{Re}_x}} = -\left(\frac{k_{Thnf}}{k_F} + Rd\left(\theta\left(0\right)\left(\theta_w - 1\right) + 1\right)^3\right)\theta'\left(0\right)\end{aligned}\right\} \tag{13}$$

where $\mathrm{Re}_x = \frac{u_w(x)x}{\vartheta_F}$ is the local Reynolds number.

Table 2 Experimental values of nanoparticles and blood [31]

Properties	Specific heat	Density	Electrical conductivity	Thermal conductivity
Blood	3594	1063	0.8	0.492
Alumina (Al_2O_3)	765	3970	36.9×10^6	40
Silicon dioxide (SiO_2)	754	2200	3.5×10^6	1.4013
Titanium oxide (TiO_2)	686.2	4250	2.4×10^6	8.9538

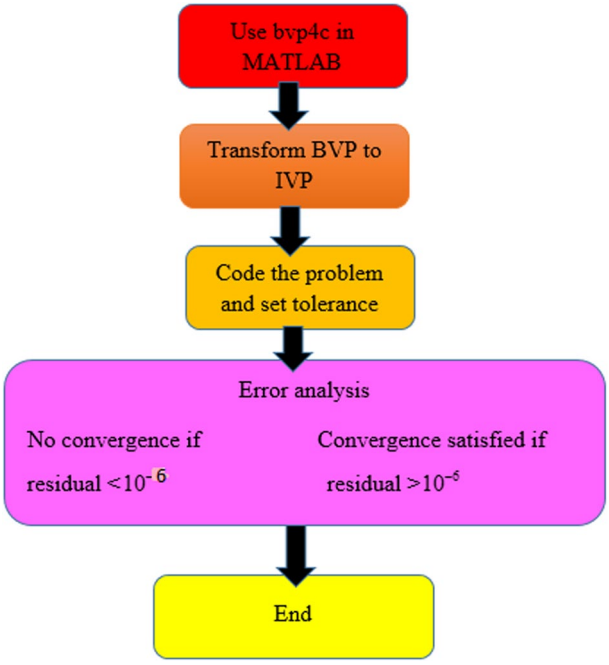


Fig. 2 Sketch of the numerical scheme

4 Numerical solution

The bvp4c solver integrates features of both colocation technique and shooting method using built in function to obtain solutions. It is widely used in different fields such as engineering, economics and fluid dynamics. The advantages of the bvp4c approach is as follows:

1. It provides reliable numerical solutions in situation where other methods are difficult to apply.
2. Through adaptive mesh refinement, it improves solution accuracy.
3. It is used for solving higher order linear and non-linear ordinary differential equations.

The following steps have been carried out to integrate the bvp4c technique in our model. Each step of the solution is given in Fig. 2.

4.1 *Step 1*:

Solve Eqs. (8–11). Let's assume a new variable;

$$\left.\begin{aligned} q_1 = F, q_2 = F', q_3 = F'', q_3' = F''', \\ q_4 = \theta, q_5 = \theta', q_5' = \theta'', \\ q_6 = \phi, q_7 = \phi', q_8' = \phi'' \end{aligned}\right\} \tag{14}$$

4.2 *Step 2*:

Using the above Eq. (14) in Eqs. (1–5), the following first order form of the ODEs by using the new variable are obtained as follows:

$$q_3' = \frac{1}{\left(\frac{\mu_{Thnf}}{\mu_f} + \beta q_3\right)} \left\{ \frac{\rho_{Thnf}}{\rho_f} \left(q_2 q_2 + q_1 q_3\right) + \frac{\sigma_{Thnf}}{\sigma_f} M q_2 + \frac{\mu_{Thnf}}{\mu_f} K p q_2 + \left(2\beta q_1 q_2 q_3\right) \right\}, \quad (15)$$

$$q_5' = \frac{\left[\begin{array}{l} -3Rd\left(\theta_w - 1\right)\left(q_4\left(\theta_w - 1\right) + 1\right)^2 q_5^2 - \frac{\sigma_{Thnf}}{\sigma_F} \Pr M E c q_2^2 \\ -\frac{(\rho C_p)_{Thnf}}{(\rho C_p)_F} \Pr q_1 q_5 + \Pr\left(N b q_5 q_7 + N t q_5^2\right) - \frac{\mu_{Thnf}}{\mu_F} \Pr E c q_3^2 - \Pr Q_a E x p\left(-n\eta\right) \end{array}\right]}{\left(\frac{k_{Thnf}}{k_F} + Rd\left(q_4\left(\theta_w - 1\right) + 1\right)^3\right)} \quad (16)$$

$$q_7' = -Sc\left(q_1 q_7 - \Omega q_6\right) - \frac{Nt}{Nb} q_5' \quad (17)$$

4.3 *Step 3*:

The subjected conditions at the boundary are:

$$\left.\begin{array}{l} q_1\left(initial\right) = 0,\ q_2\left(initial\right) - 1,\ \frac{k_{Thnf}}{k_f} q_5\left(initial\right) + BiT\left(1 - q_4\left(initial\right)\right) \\ q_7\left(initial\right) + Bc\left(1 - q_6\left(initial\right)\right) - 0 \\ q_2\left(final\right) - 0,\ q_4\left(final\right) - 0,\ q_6\left(final\right) - 0 \end{array}\right\} \quad (18)$$

4.4 *Step 4*:

Apply the boundary condition in Eq. (18) and Eqs. (16–17) are coded in bvp4c solver.

4.5 *Step 5*:

While using bvp4c, two different set of initial guesses are applied to obtain the solution. The relative tolerance and absolute tolerance are set to (= 10–6) for the outcome shows the guarantee of precise numerical solution. If the results satisfy Eq. (11), the selected initial guess is acceptable. Otherwise, the process is repeated using other set of initial guesses.

5 Validation

This section presents the validity of the approach employed in the present study, the value of $\theta'(0)$ across a variation in values of $\Pr$ was compared to the published work of Abas et al. [55] and Hamad et al. [57] the outcomes are shown in Table 3. The results show smooth agreement and confirm the accuracy of the procedure.

Table 3 Comparison of Nusselt number with published work

Pr		**0.2**	**2.0**	**7.0**
$\theta'(0)$	Abas et al. [55]	−0.16913	−0.91145	−1.89545
	Hamad et al. [57]	−0.16910	−0.91142	−1.89537
	Present	−0.169100	−0.911436	−1.900210

6 Discussion

This section presents a comprehensive analysis of the findings, emphasizing the influence of the different physical factors, which are, Porosity parameter $(= Kp)$, magnetic parameter is $(= M)$, Maxwell parameter $(= \beta)$, thermal radiation $(= Rd)$, heat source $(= Q_a)$, Eckert number $(= Ec)$, Schmidt number $(= Sc)$, Biot number $(= BiT)$, chemical reaction parameter $(= \Omega)$, and concentration Biot number $(= Bc)$ on velocities $(= F'(\eta))$, temperature $(= \theta(\eta))$, and concentration $(= \phi(\eta))$ distributions. The results are illustrated through graphical representations for ternary hybrid nanofluid flow $(Al_2O_3 + SiO_2 + TiO_2/Blood)$ and hybrid nanofluid flow $(Al_2O_3 + SiO_2/Blood)$ profiles.

6.1 Velocity profile

Figure 3 illustrates the effects of M on $F'(\eta)$ and temperature distribution for $(Al_2O_3 + SiO_2 + TiO_2/Blood)$ and $(Al_2O_3 + SiO_2/Blood)$. The elevated M parameter diminishes $F'(\eta)$ profile for $(Al_2O_3 + SiO_2 + TiO_2/Blood)$ and $(Al_2O_3 + SiO_2/Blood)$. Growth in M improves the interaction of the fluid particles and magnetic field. This interaction generates a Lorentz force that acts to the opposite to the flow direction. This resistive force impedes the migration of the nanoparticles and reduces the thickness of the boundary layer. Consequently, the $F'(\eta)$ distribution for $(Al_2O_3 + SiO_2 + TiO_2/Blood)$ and $(Al_2O_3 + SiO_2/Blood)$ diminishes. This increment in $F'(\eta)$ is more significant for $(Al_2O_3 + SiO_2 + TiO_2/Blood)$.The impact of Kp on $F'(\eta)$ profile of $(Al_2O_3 + SiO_2 + TiO_2/Blood)$ and $(Al_2O_3 + SiO_2/Blood)$, is seen in Fig. 4. As the porous factor Kp grows, $F'(\eta)$ distributions decreases for both $(Al_2O_3 + SiO_2 + TiO_2/Blood)$ and $(Al_2O_3 + SiO_2/Blood)$ because fluids encounter more resistance while flowing through porous material. The density or limiting porosity

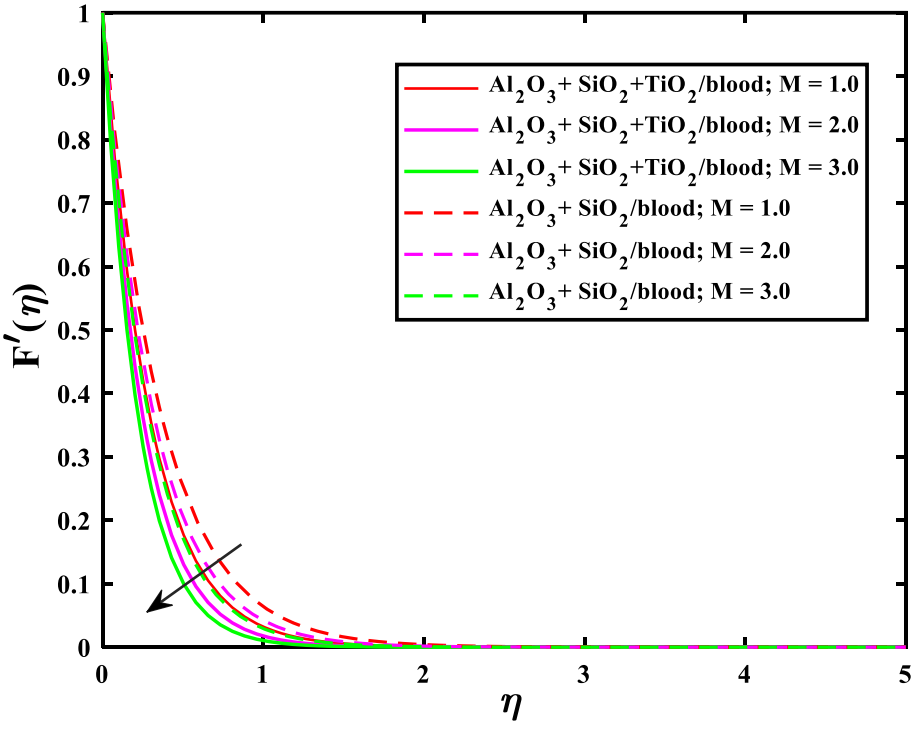


Fig. 3 Velocity profile for varying M

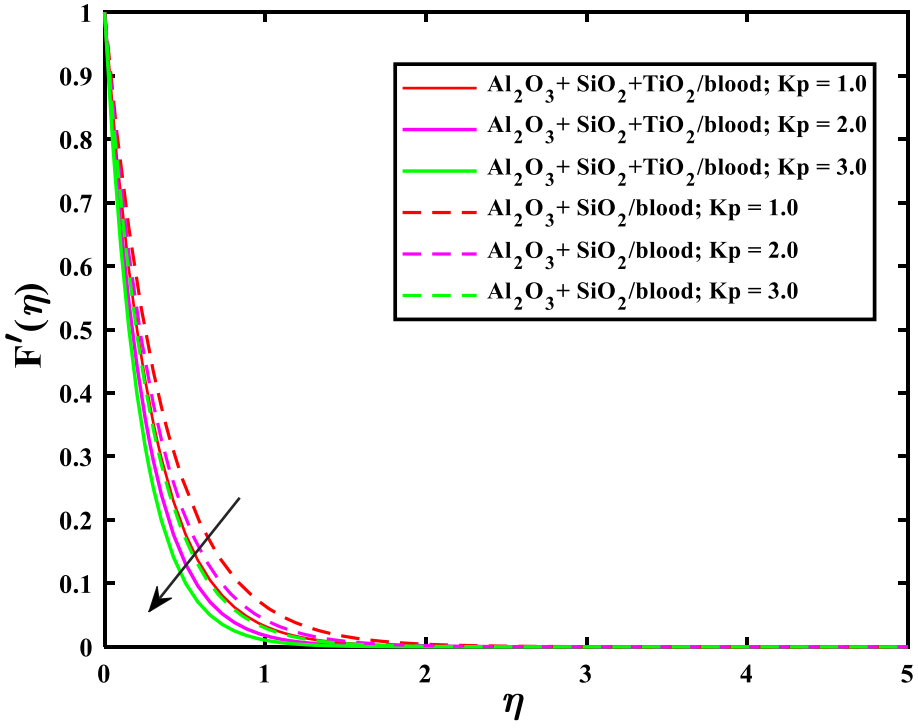


Fig. 4 Velocity profile for varying Kp

of a medium is indicated by its porosity factor, which in turn increases the frictional resistance between the solid matrix and the fluid, resulting in a decrease in the fluid's velocity. In comparison to $(Al_2O_3 + SiO_2 + TiO_2/Blood)$ and $(Al_2O_3 + SiO_2/Blood)$ nanofluids, ternary hybrid nanofluid $(Al_2O_3 + SiO_2 + TiO_2/Blood)$ shows a quicker fall in $F'(\eta)$ profile as Kp increases, due to its larger nanoparticle content. Figure 5 demonstrates the impression of β on $F'(\eta)$. Growth in β reduces the $F'(\eta)$ profiles for $(Al_2O_3 + SiO_2 + TiO_2/Blood)$ and $(Al_2O_3 + SiO_2/Blood)$. The increasing values of β amplify the stress relaxation phenomena, which resist deformation and slows momentum transfer, therefore diminishing velocity $F'(\eta)$, as shown in Fig. 5.

6.2 Temperature profile

The impression of M on $\theta(\eta)$ is displayed in Fig. 6. Growth in M heightens the $\theta(\eta)$ distributions for $(Al_2O_3 + SiO_2 + TiO_2/Blood)$ and $(Al_2O_3 + SiO_2/Blood)$. Actually, enhance the M parameter strengthens the applied magnetic field and increase the interaction of the magnetic field and electrically conducting fluid. This interaction produce additional Joule heating due to the electrical resistance in the fluid. As a result, more energy is generated within the boundary layer, hence increasing $\theta(\eta)$. Figure 7 depicts the influences of Ec on $\theta(\eta)$ for $(Al_2O_3 + SiO_2 + TiO_2/Blood)$ and $(Al_2O_3 + SiO_2/Blood)$. Growth in Ec escalates the $\theta(\eta)$ distribution of the $(Al_2O_3 + SiO_2 + TiO_2/Blood)$ and $(Al_2O_3 + SiO_2/Blood)$. Eckert number is defined as the ratio of kinetic energy to the change in enthalpy. Therefore, the kinetic energy grows with the value of Ec. The nanofluid system's temperature rises due to the friction generates with the motion of the fluid as a result internal energy of the fluid amplified. Consequently, the thermal profile accelerates. Additionally, the higher result is observed for $(Al_2O_3 + SiO_2 + TiO_2/Blood)$. Figure 8 portrays the influences of BiT

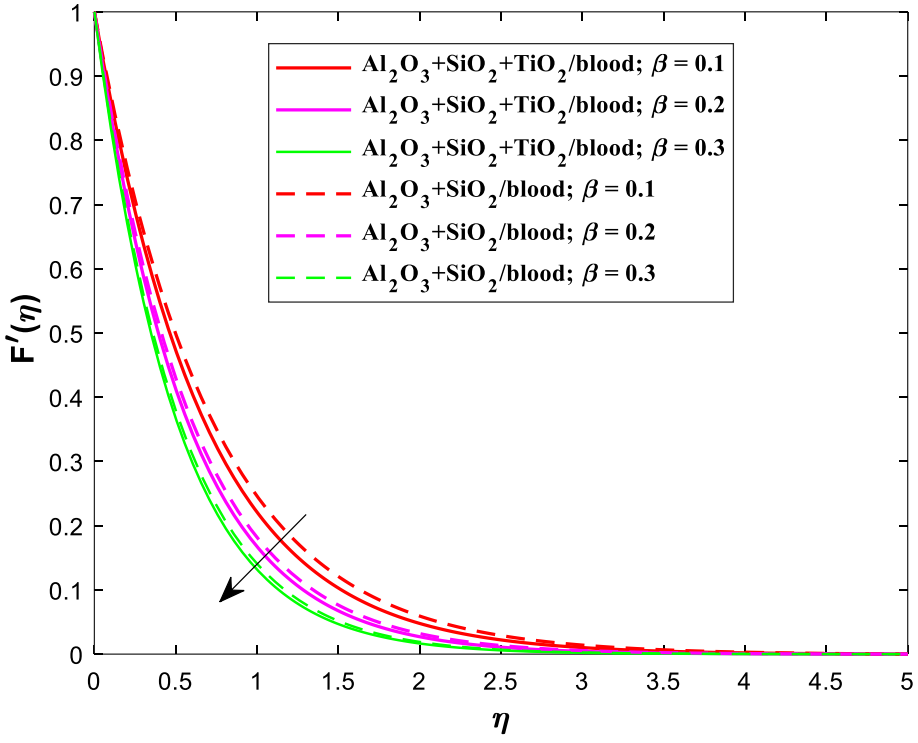


Fig. 5 Velocity profile for varying β

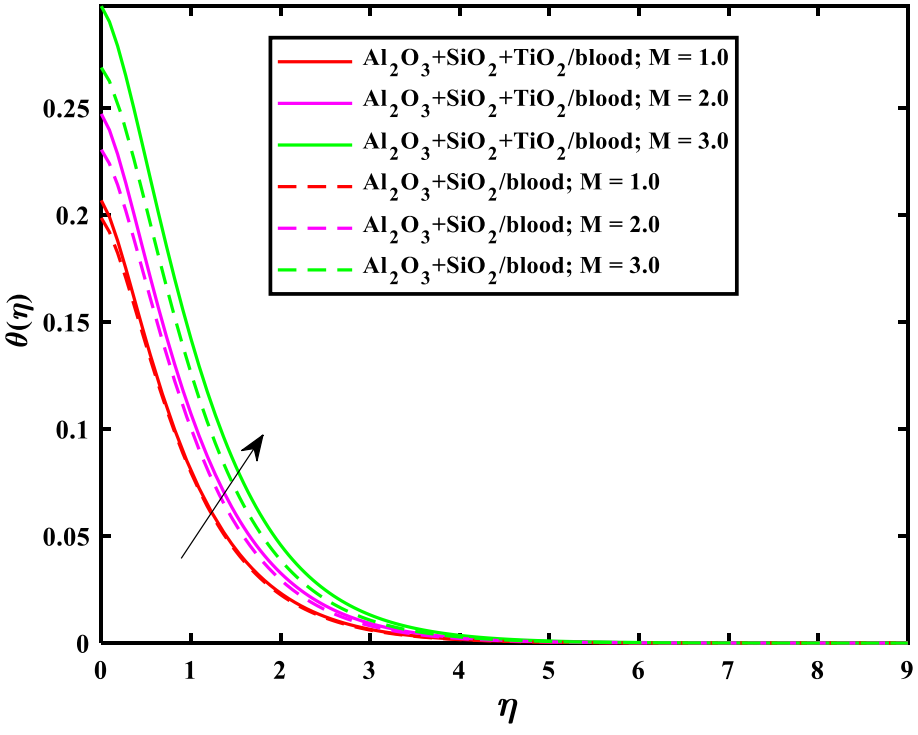


Fig. 6 Temperature profile for varying M

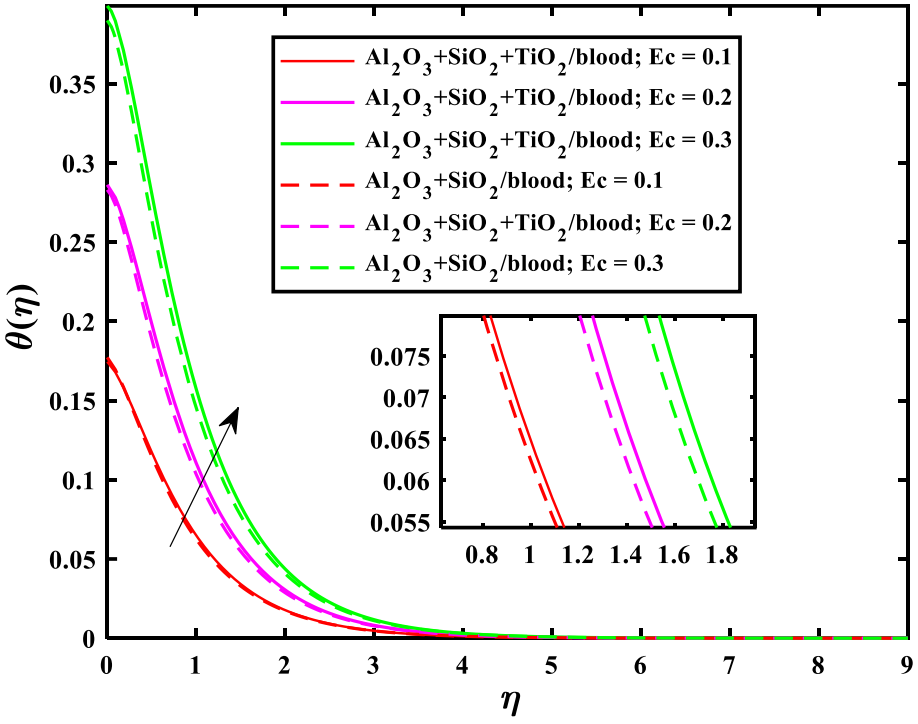


Fig. 7 Temperature profile for varying Ec

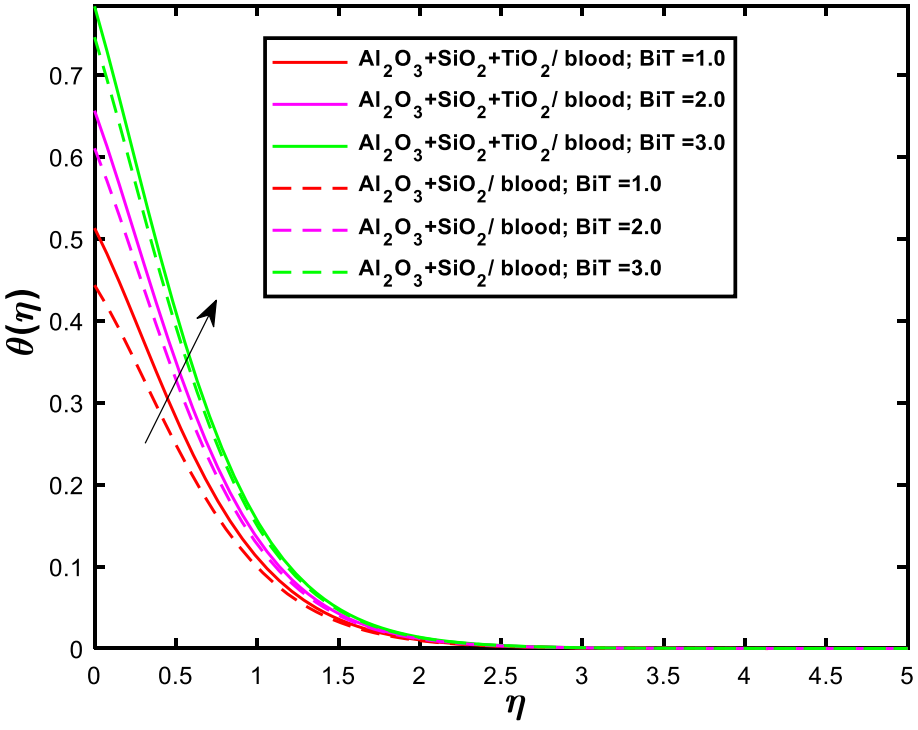


Fig. 8 Temperature profile for varying BiT

on $\theta(\eta)$ of $(Al_2O_3 + SiO_2 + TiO_2/Blood)$ and $(Al_2O_3 + SiO_2/Blood)$ nanofluid. Upsurge BiT boosts $\theta(\eta)$. The thermal transfer of nanoparticles towards boundary layers is facilitated by an increase in the thermal and heat transfer rate, which occurs when h_F increased. As a result the surface becomes more effective in transferring heat, a larger amount of thermal energy enters the fluid. This escalates the $\theta(\eta)$ distribution and thickens the thermal boundary layer. The impact of BiT on $\theta(\eta)$ is slightly greater for $(Al_2O_3 + SiO_2 + TiO_2/Blood)$. Figure 9 shows the impression of Rd on $\theta(\eta)$ profile of $(Al_2O_3 + SiO_2 + TiO_2/Blood)$ and $(Al_2O_3 + SiO_2/Blood)$. From this Figure, it is found that growth in Rd boosts the temperature distribution. In a physical sense, a higher Rd increases the rate of heat transmission by widening the thermal layer at the boundary, which in turn increases $\theta(\eta)$. Furthermore, the greatest increase in found for $(Al_2O_3 + SiO_2 + TiO_2/Blood)$ nanofluid flow profile. The influences of Q_a on $\theta(\eta)$ is depicted in Fig. 10. The increasing Q_a escalates the $\theta(\eta)$ distributions of $(Al_2O_3 + SiO_2 + TiO_2/Blood)$ and $(Al_2O_3 + SiO_2/Blood)$. The space-dependent heat source factor characterizes the special fluctuations in heat generation within the fluid. As this factor escalates, the special distribution of the generation becomes more prominent, which in turn improves the fluid flow over a stretching surface. This increasing effect is higher for $(Al_2O_3 + SiO_2 + TiO_2/Blood)$. The same increasing effects are seen in Fig. 11 for $\theta(\eta)$ via θ_w. The increasing θ_w, improves the heat of the fluid, and consequently intensity the $\theta(\eta)$ profile for $(Al_2O_3 + SiO_2 + TiO_2/Blood)$ and $(Al_2O_3 + SiO_2/Blood)$.

6.3 Concentration profile

Figure 12 illustrates the influence of Sc on $\phi(\eta)$ profile. An increasing Sc diminishes the $\phi(\eta)$ profile for $(Al_2O_3 + SiO_2 + TiO_2/Blood)$ and $(Al_2O_3 + SiO_2/Blood)$. The

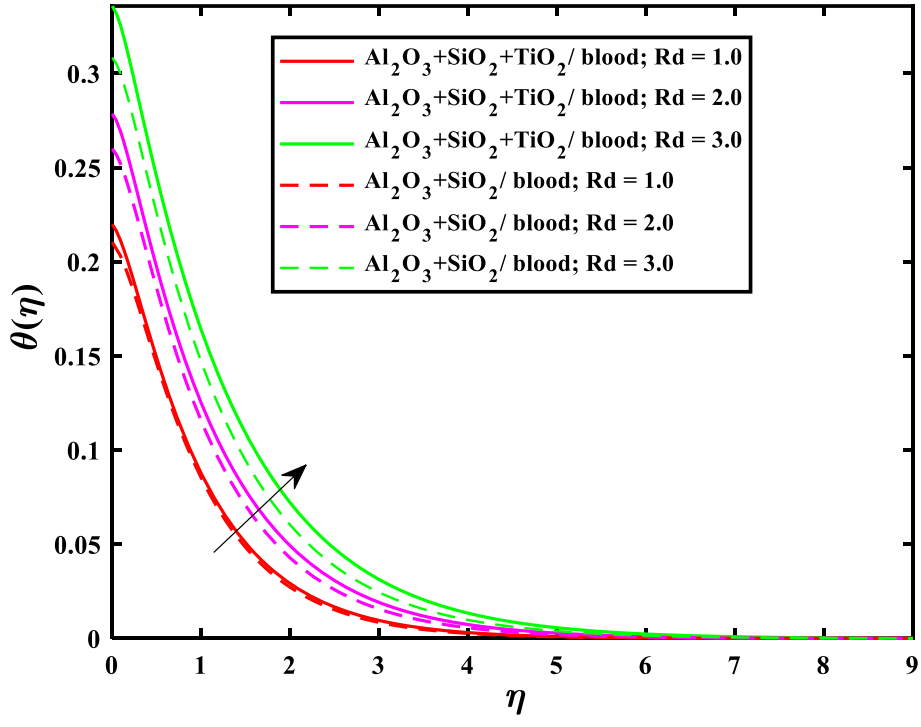


Fig. 9 Temperature profile for varying Rd

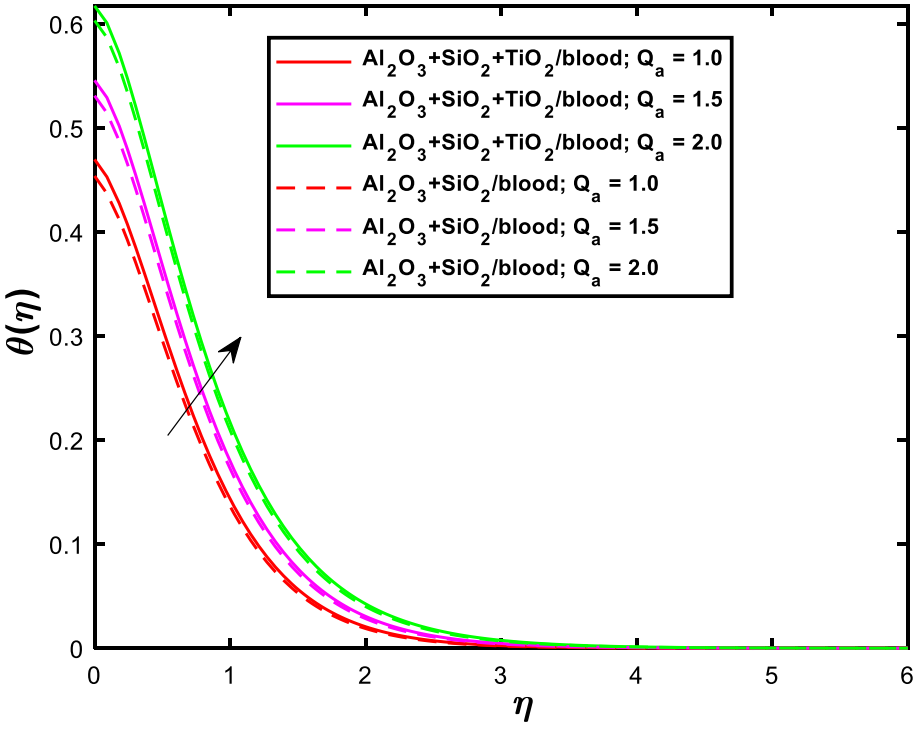


Fig. 10 Temperature profile for varying Q_a

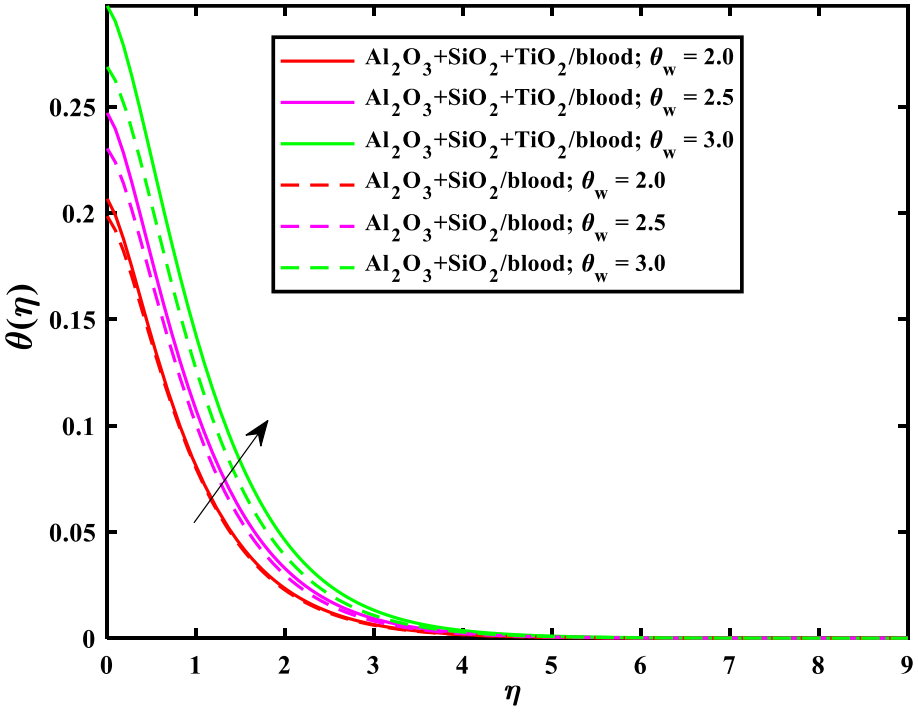


Fig. 11 Temperature profile for varying θ_w

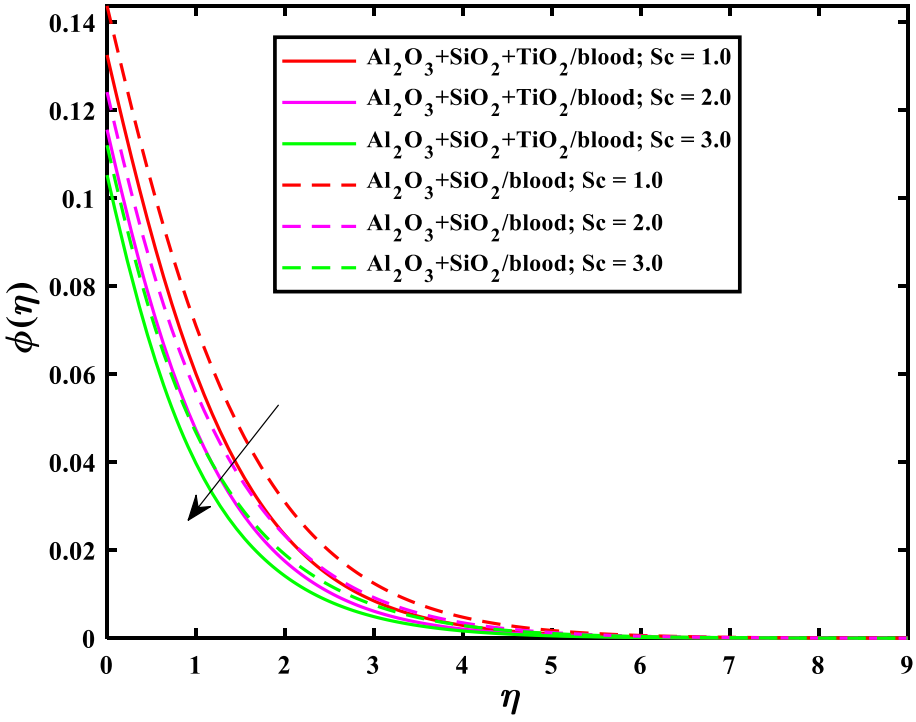


Fig. 12 Concentration profile for varying Sc

Schmidt number is defined as the ratio of kinematic viscosity to mass diffusivity. A high Schmidt number indicates that the mass diffusivity is low compared to the momentum diffusivity, signifying slow particle dispersion within the fluid. As Sc increases, the particles encounter greater difficulty in diffusing throughout the fluid, resulting in a diminished concentration at the boundary layer. This decreasing effect is dominant for $(Al_2O_3 + SiO_2 + TiO_2/Blood)$. Figure 13 illustrates the impression of Ω on $\phi(\eta)$ of both $(Al_2O_3 + SiO_2 + TiO_2/Blood)$ and $(Al_2O_3 + SiO_2/Blood)$ nanofluids. Growth in Ω lessen $\phi(\eta)$ profiles for $(Al_2O_3 + SiO_2 + TiO_2/Blood)$ and $(Al_2O_3 + SiO_2/Blood)$. Actually, increase in Ω parameter enhances the consumption of species due to the stronger reaction effects. This phenomenon, reduces the concentration of the fluid particles within the boundary layer. Figure 14 illustrates the effect of Bc on $\phi(\eta)$ of the $(Al_2O_3 + SiO_2 + TiO_2/Blood)$ and $(Al_2O_3 + SiO_2/Blood)$. Upsurge in Bc amplifies $\phi(\eta)$. The bigger Bc is directly related to the mass transfer coefficient h_B. A higher Bc enhanced mass transfer efficiency between the surface and fluid, resulting in a more substantial mass exchange. Consequently, the nanofluid adjacent to the surface attains a higher concentration, thereby enhancing the overall $\phi(\eta)$ distribution for $(Al_2O_3 + SiO_2 + TiO_2/Blood)$ and $(Al_2O_3 + SiO_2/Blood)$ inside the system. Moreover, impact of Bc is slightly better for $(Al_2O_3 + SiO_2 + TiO_2/Blood)$.

6.4 Table discussion

Table 1 shows the theoretical models of the thermophysical properties of the nanoparticles. Table 2 provides the numerical values of the nanoparticles and base fluid. The validation of the code with published work is shown in Table 3. Table 4 shows the consequences of varying values of,M,Kp and β on skin friction coefficient of $(Al_2O_3 + SiO_2/Blood)(Al_2O_3 + SiO_2 + TiO_2/Blood)$. Increasing M, β and Kp

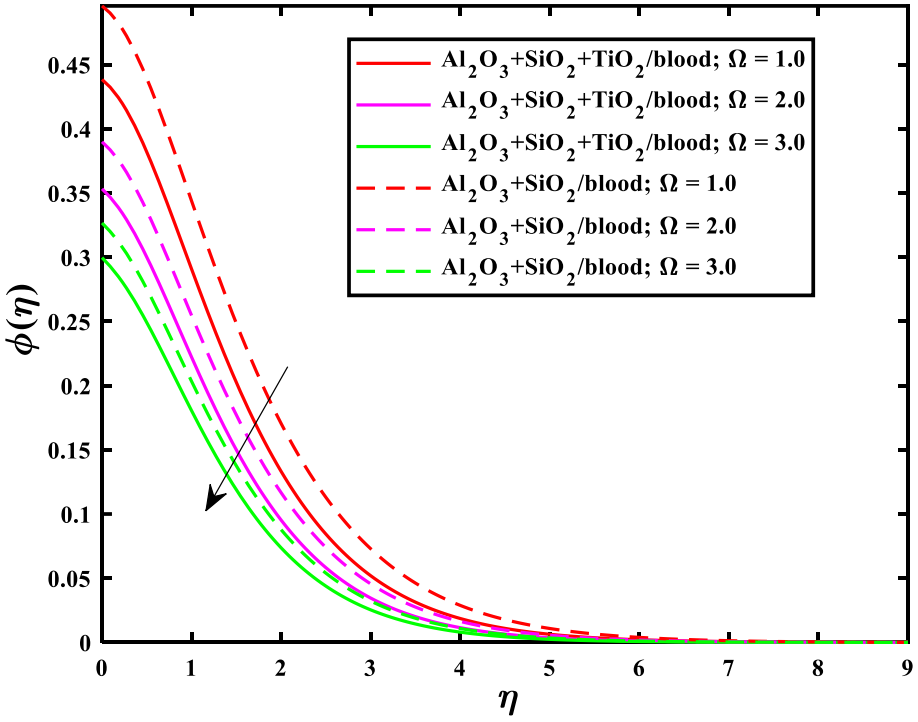


Fig. 13 Concentration profile for varying Ω

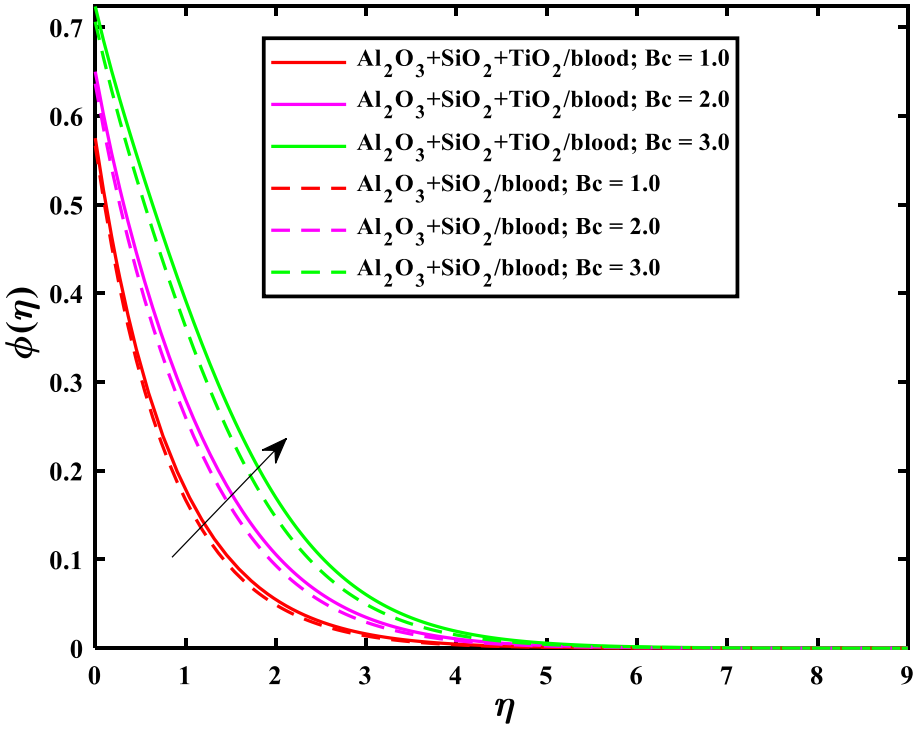


Fig. 14 Concentration profile for varying Bc

Table 4 Skin friction via M,Kp and β

M	Kp	β	Skin friction	
			Hybrid nanofluid	Ternary hybrid nanofluid
1.5	0.6		1.2531	1.37841
2.0			1.2668	1.39348
2.5			1.2795	1.40105
1.0	1.0		1.1639	1.2221
	1.3		1.1871	1.2464
	1.6		1.2108	1.2713
			1.5863	1.6354
			1.6188	1.6189
			1.6520	1.7032

Table 5 Nusselt number for varying values of Rd,Q_a,θ_w and BiT

Rd 2	Q_a 1	θ_w 1.5	BiT 2.2	Nusselt number	
				Hybrid nanofluid	Ternary hybrid nanofluid
1.0	0.6	1.2	0.8	2.4315	2.4801
2.0				2.4558	2.5049
3.0				2.4804	2.5300
	0.8			2.1920	2.2139
	0.9			2.2029	2.2249
	1.0			2.2139	2.2350
		1.5		1.3956	1.4165
		2.0		1.4374	1.4589
		2.5		1.4805	1.5027
			1.0	1.8937	1.9353
			1.1	1.9599	2.0030
			1.2	2.0285	2.0731

values enhances the skin friction coefficient for both $(Al_2O_3 + SiO_2/Blood)$ and $(Al_2O_3 + SiO_2 + TiO_2/Blood)$ nanofluid. Physically, magnetic filed enhances the Lorentz force opposing the flow, which enhances the resistance near the surface and hence increase skin friction. Furthermore, β elastic effect which resist deformation Kp increases drag force due to porous medium restrict the fluid on the surface, resulting in higher skin friction. Table 5 portrays the influences of Rd,Q_a,θ_w, and BiT on Ns. From this table it is noted that Ns intensified against all these parameters. A rise in Rd enhances radiative heat energy within the fluid, intensifying heat transfer from the surface. Heat source parameter Q_a supplies additional thermal energy to the fluid, which strengthens the temperature gradient at the surface and improves Ns. Higher θ_w intensifies the thermal driving force between the surface and the fluid, as a results Ns raise. An increase in BiT shows convective heat exchange at the surface, allowing more heat to be transferred to the fluid, which results in higher Ns. Additionally, the greatest growing behavior is observed for $(Al_2O_3 + SiO_2 + TiO_2/Blood)$ nanofluid. The computational evaluations of Sw for different values of Sc,Ω and Bc are presented in Table 6. This table shows that Sw improves more for $(Al_2O_3 + SiO_2 + TiO_2/Blood)$ against the growing estimation of Bc whereas lessens for Sc and Ω. Actually, h_B represents the mass transfer coefficient, which is directly linked with Bc. Larger number of Bc improve the mass transfer rate by promoting greater diffusion of species into the fluid. A higher Sc values reduces the mass diffusivity, which weakens the species diffusion and lowers the mass transfer rate. Moreover, growing values of Ω improves spcies consumption within the

Table 6 Sherwood number for different values of Sc, Bc and Ω

Sc	Bc	Ω	Sherwood number	
			Hybrid nanofluid	Ternary hybrid nanofluid
1.0	0.7	0.2	1.8543	1.8361
1.5			1.8581	1.8397
2.0			1.8618	1.8434
	1.0		1.2934	1.3322
	1.2		1.3063	1.3454
	1.4		1.3193	1.3589
		0.8	1.5762	1.5438
		0.9	1.5951	1.5623
		1.0	1.6142	1.5810

boundary layer, reducing concentration gradients at the wall and consequently diminishing the Sw.

7 Conclusion

In this section investigate the blood-based ternary hybrid Maxwell nanofluid flow past an enlarging porous sheet. The nanoparticle alumina, Titanium oxide and silicon dioxide are mixed in blood to hybridize the fluid. It is also vital to note that the combined effects of the nonlinear thermal radiation and an exponential space-based heat source are also considered. The reduced form of the equations evaluated by bvp4c. The major discoveries of the present study are as follows:

- The reducing trend has been noted in velocity distribution with larger values of magnetic, porosity and Maxwell parameters.
- Improving the concentration Biot number results in high concentration profile, while a reducing impression is seen for mounting values of Schmidt number and chemical reaction parameters.
- Thermal distribution is enhanced with the growth in Eckert number, magnetic parameter, Biot number, thermal radiation and heat source factors.
- Using ternary hybrid nanofluid, the magnetic, porosity and Maxwell parameters increased the skin friction coefficient
- Nusselt number of ternary hybrid and hybrid nanofluids improved for thermal radiation, heat source, temperature difference parameter and Biot number.
- To strengthen the values of concentration Biot number, the Sherwood number for ternary hybrid nanofluid improves while decline against higher values of chemical reaction and Schmidt number.

7.1 Future work

In future, this work can be extended by considering different kinds of nanoparticles, different non-Newtonian model, and different base fluids like kerosene oil and sodium alginate etc. to present industrial applications. Moreover, the velocity, thermal and concentration slip constraints can be adopted to study the slip flow by different kinds of nanofluids.

7.2 Applications

This study offers significant applications in targeted drug delivery systems, bio medical engineering, and blood flow analysis in medical devices. The findings are applicable to

electromagnetic heating control, biochemical processing, advanced thermal management in engineering processes involving non-Newtonian and electrically conducting fluids.

List of symbols

B_0	Magnetic field strength (N/Am)
a	Positive constant (–)
D_T	Thermophoresis diffusion coefficient (m^2/s K)
M	Magnetic field (–)
ϑ	Kinematic viscosity (m^2/s)
$x-, y-$	Cartesian coordinates (m)
β	Maxwell fluid parameter (–)
Q_a	Heat source (–)
θ_w	Temperature difference parameter (–)
D_B	Brownian diffusion coefficient (m^2/s)
T	Temperature (K)
u, v	Velocity components (m/s)
q_r	Radiative heat flux (W/m^2)
SF_x	Skin fraction coefficient (–)
Rd	Thermal radiation (–)
Pr	Prandtl number (–)
Kp	Porosity parameter (–)
σ	Electrical conductivity (s/m)
h_F	Heat transfer coefficient (W/m^2 K)
T_F	Reference temperature (K)
Sw	Sherwood number (–)
Nt	Thermophoresis parameter (–)
h_B	Mass transfer coefficient
$\varphi_{s(1,2,3)}$	Nanoparticle volume fractions (–)
ρ	Density (kg/m^3)
C_p	Heat capacitance (j/kg K)
Nb	Brownian parameter (–)
Ns	Nusselt number (–)
μ	Dynamic viscosity (kg/m s)
Ω	Chemical reaction parameter (–)
C	Concentration of the fluid (kg/m^3)
T_∞	Ambient temperature (K)
C_w	Surface concentration (kg/m^3)
σ	Electrical conductivity (1/Ω m)
σ_e	Stefan–Boltzmann constant (W/m^2 K^4)
k	Thermal conductivity (W/m K)
k_e	Mean absorption coefficient (1/m)
η	Similarity variable (–)

Subscripts

F	Base fluid (–)
nf	Nanofluid (–)
hnf	Hybrid nanofluid (–)
$s1, s2, s3$	First, second and third nanoparticle (–)
$Thnf$	Ternary hybrid nanofluid (–)
∞	Situation in free stream (–)

Abbreviations

MHD	Magnetohydrodynamic
ODE	Ordinary differential equation
PDE	Partial differential equation
BVP	Boundary value problem
IVP	Initial value problem

Author contributions

Ibrahim Mahariq: advanced analytical guidance, interpretation of results, assistance in simulation analysis, and manuscript editing, Visualization, Syed Arshad Abas: Conceptualization, methodology development, mathematical modeling, formal analysis, and initial draft preparation. Mehreen Fiza: Numerical simulations, data curation, visualization, and validation of results. Software, Hakeem Ullah: Literature review, Supervision, Project administration, resources; Ali Akgül: Methodology refinement, technical support for numerical techniques, and substantial review and editing of the manuscript. Validation, Mukhlisa Soliyeva: Contribution to physical modeling, discussions on heat transfer aspects, and verification of numerical procedures. Hasan AKSOY: contributed during the revision stage by improving the theoretical formulation, validating the numerical results, revising the manuscript in response to reviewers' comments, and enhancing the discussion of physical interpretations and proof reading of paper. Seham M. Al-Mekhlafi: refinement of the mathematical formulation, Visualization, and final approval of the manuscript.

Funding
The authors received no funding for this research.

Data availability
Data is provided within the manuscript.

Declarations

Ethics approval and consent to participate
Not applicable.

Consent for publication
Not applicable.

Competing interests
The authors declare no competing interests.

Author details
[1]Najjad Zeenni Faculty of Engineering, Al-Quds University, Jerusalem, Palestine
[2]Department of Electrical and Electronic Engineering, Faculty of Engineering and Architecture, Istanbul Gelisim University, 34310 Avcılar-Istanbul, Istanbul, Türkiye
[3]University College, Korea University, Seoul 02481, South Korea
[4]Department of Medical Research, China Medical University Hospital, China Medical University, Taichung, Taiwan
[5]Department of Mathematics, Abdul Wali Khan University, Mardan 23200, Khyber Pakhtunkhwa, Pakistan
[6]Department of Electronics and Communication Engineering, Saveetha School of Engineering, SIMATS, Chennai, Tamilnadu, India
[7]Department of Electrical and Electronics Engineering, Faculty of Engineering, Karadeniz Technical University, Trabzon, Türkiye
[8]Art and Science Faculty, Department of Mathematics, Siirt University, 56100 Siirt, Türkiye
[9]Applied Science Research Center, Applied Science Private University, Amman, Jordan
[10]Department of Physics and Teaching Methods, National Pedagogical University of Uzbekistan, Tashkent, Uzbekistan
[11]Department of Electrical and Electronics Engineering, University of Turkish Aeronautical Association, Ankara, Türkiye
[12]Department of Mathematics, Sana'a University, Sana'a, Yemen

Received: 29 November 2025 / Accepted: 1 March 2026
Published online: 15 April 2026

References

1. Li Y, Xia Y, Deng W, Gao X, Li H, Gao X. Nucleate boiling heat transfer and critical heat flux in controllable droplet trains cooling. Appl Therm Eng. 2025;267:125824.
2. Moghimi SM, Hosseinzadeh K, Hasibi A. Investigation of nanofluid flow in the channel under effect of magnetic field and Joule heating. Case Stud Therm Eng. 2024;55:104152.
3. Sarfraz M, Muhammad K, Alrihieli HF, Abdelmohimen MAH. Heat and mass transfer analysis in flow of Walter's B nanofluid: A numerical study of dual solutions. ZAMM J Appl Math Mech Für Angew Math Und Mech. 2025;105:e202300951.
4. Fu C, Huang K, Chen H, Huang B, Zhang W. From fundamental mechanisms to applications and challenges of nanofluid flooding in enhanced oil recovery: a review. Fuel. 2025;396:135317.
5. Razzaq I, Xinhua W, Rasool G, Sun T, Thumma T, Reddy CA, et al. Effects of viscous and Joule dissipation on hydromagnetic hybrid nanofluid flow over nonlinear stretching surface with Hamilton-Crosser model. Case Stud Therm Eng. 2024;61:105125.
6. Panda S, Ontela S, Pattnaik PK, Mishra SR. Radiating heat effect on powell–eyring blood-based hybrid nanofluid over a riga plate with thermal stratification CattaneoChristov heat flux model. Partial Differ Equ Appl Math. 2024;11:100769.
7. Hu X, Quan B, Shi Z, Zhao X, Lu G, Ding Y, Lai J, Qu J, Peng Y, Lu X. Bioinspired Hierarchical Radiative-Phase Change Hybrid Cooling Composite with Record-Breaking Cooling Power. Adv Mater. 2025; e10988
8. Mahmood Z, Duraihem FZ, Adnan, Khan U, Hassan AM. Model-based comparative analysis of MHD stagnation point flow of hybrid nanofluid over a stretching sheet with suction and viscous dissipation. Numer Heat Transf Part B Fundam 2024; 1–22
9. Yasir M, Khan M, Alqahtani AS, Malik MY. Heat generation/absorption effects in thermally radiative mixed convective flow of Zn– TiO_2/H_2O hybrid nanofluid. Case Stud Therm Eng. 2023;45:103000.
10. Urooj A, Hassan QMU, Raja MAZ, Ayub K, Nisar KS, Shoaib M. Numerical treatment for radiative hybrid nanofluid flow over a stretching sheet. Results Eng. 2024;22:102209.
11. Ai C, Liu C, Sun P, Liu C. Na_2CO_3-SiO_2-H_2O nanofluid synergistically treats coal dust and hydrogen sulfide. J Environ Chem Eng 2025; 119365
12. Muhammad K, Sarfraz M. Regression analysis of squeezing-induced hybrid nanofluid flow in Darcy-Forchheimer porous medium. Appl Math Mech. 2025;46:193–208.
13. Abas SA, Ullah H, Fiza M, Jan AU, Akgül A, Hendy AS, et al. Effects of Joule heating on MHD flow of hybrid nanofluid between rotating disks. J Radiat Res Appl Sci. 2025;18:101341.
14. Muhammad K, Sarfraz M, Ebaid A, Elmannai H. Optimization of energy transport via electro-thermal hybrid nanofluid in parallel disks: a Keller-Box simulation. Chaos Solitons Fractals. 2025;198:116621.

15. Gangadhar K, NagaChandrika G, Dinarvand S. Stagnation point of the triple nanoparticle nanofluid flow through the spinning sphere with radiation absorption. Pramana. 2024; 98 95
16. Sireesha S, Gangadhar K, Dinarvand S. Comparative energy performance in Au/H2O, Au–Ag/H2O and Au–Ag–MWCNT/H2O with shape factor with heat generation impact. Mod Phys Lett B. 2025; 2550183
17. Varatharaj K, Tamizharasi R, Vajravelu K. Ternary hybrid nanofluid flow and heat transfer at a permeable stretching sheet with slip boundary conditions. Eur Phys J Spec Top. 2025;234:2293–316.
18. Yasir M, Alroobaea R, Ahammad NA, Elseesy IE. Melting heat transport reliability on dynamics of tri-hybrid nanofluid due to inclined shrinking surface. Case Stud Therm Eng. 2025;70:106059.
19. Thamizhselvi V, Venkateswarlu B, Misra A, SatyaNarayana PV, Harish BD. Numerical simulation of Jeffrey ternary nanofluid flow over an exponential stretching sheet with inclined magnetic field and heat source. Multiscale Multidiscip Model Exp Des. 2025;8:386.
20. Mahboobtosi M, Hosseinzadeh K, Najafpour A, Ganji DD. Entropy generation analysis of kerosene oil flow with ternary hybrid nanoparticles on the stretchable exponential surface. Int J Model Simul 2024; 1–15
21. Yasir M, Khan M, Alansari M, Ullah MZ. Exploration of motion of methanol experiencing alumina and silica nanoparticles with emphasis on multiple solutions. Alexandria Eng J. 2023;83:367–75.
22. Moltot AT, Gorfie EH, Zergaw GA, Asress HD. Influences of variable thermal conductivity, viscous dissipation, and Cattaneo–Christov heat and mass fluxes on MHD tangent hyperbolic ternary hybrid nanofluid flow over a stretching sheet. Eng Reports. 2025;7:e70291.
23. Mahboobtosi M, Hosseinzadeh K, Ganji DD. Investigating the convective flow of ternary hybrid nanofluids and single nanofluids around a stretched cylinder: parameter analysis and performance enhancement. Int J Thermofluids. 2024;23:100752.
24. Shamshuddin MD, Panda S, Salawu SO, Mishra SR, Patil VS. Analysis of Casson ternary nanofluid integration under various thermal physical impacts with Cattaneo-Christov model: exploring magnified heat transfer in stretchy surface. Int J Hydrog Energy. 2025;101:450–60.
25. BinTurabi YUU, Munir S, Amin A. Numerical analysis of convective transport mechanisms in two-layer ternary (TiO 2– SiO 2– Al 2 O 3) casson hybrid nanofluid flow in a vertical channel with heat generation effects. Numer Heat Transf Part A Appl. 2025;86:1673–87.
26. Priyadharshini P, Archana MV, Shah NA, Alshehri MH. Ternary hybrid nanofluid flow emerging on a symmetrically stretching sheet optimization with machine learning prediction scheme. Symmetry. 2023;15:1225.
27. Alanazi MM, AhmedHendi A, Ahammad NA, Ali B, Majeed S, Shah NA. Significance of ternary hybrid nanoparticles on the dynamics of nanofluids over a stretched surface subject to gravity modulation. Mathematics. 2023;11:809.
28. Shah SZH, Wahab HA, Khan S, Alderremy AA, Mahmoud EE. Optimization of nanoscale heat transport analysis of ternary hybrid nanofluid over three-dimensional wedge geometry in magnetized environment. ZAMM J Appl Math Mech Für Angew Math Und Mech. 2025;105:e202400064.
29. Khan SA, Imran M, Waqas H, Muhammad T, Yasmin S, Alhushaybari A. Numerical analysis of multiple slip effects on CuO/MgO/TiO2-water ternary hybrid nanofluid with thermal and exponential space-based heat source. Tribol Int. 2024;197:109778.
30. Shamshuddin MD, Panda S, Saeed A, Ratha PK, Mishra SR. Homotopy analysis on magnetized Williamson-micropolar nanofluid flow over a bi-directionally extending surface with multiple slip conditions. Numer Heat Transf Part B Fundam. 2025;86:3696–716.
31. Lone SA, Khan A, Raiza Z, Alrabaiah H, Shahab S, Saeed A, Bonyah E. A semi-analytical solution of the magnetohydrodynamic blood-based ternary hybrid nanofluid flow over a convectively heated bidirectional stretching surface under velocity slip conditions. AIP Adv 2024; 14
32. Alsoufi MMO, Gangadhar K, Chamkha AJ. MgO-ZnO-Au tri-nanohybrid fluid flow across an artery with uses of the respiratory system's blood circulation and medication delivery. Mod Phys Lett B. 2026;40:2650022.
33. Shamshuddin MD, Salawu SO, Panda S, Mishra SR, Alanazy A, Eid MR. Thermal case exploration of electromagnetic radiative tri-hybrid nanofluid flow in bi-directional stretching device in absorbent medium: SQLM analysis. Case Stud Therm Eng. 2024;60:104734.
34. Sarfraz M, Muhammad K. Numerical solutions for thermal and solutal transport of Jeffrey fluid flow subject to rotation via Keller-Box method. Multiscale Multidiscip Model Exp Des. 2025;8:177.
35. Bilal S, Yasir M. Mass transpiration impact on effectiveness of heat transport of ternary hybrid nanofluid with velocity slip, Case Stud. Therm Eng 2025; 106530
36. Madiha Takreem K, Satya Narayana PV. Impacts of Joule heating and dissipation on magnetohydrodynamic ternary-hybrid nanofluid (A l 2 O 3-T i O 2-S i O 2/H 2 O) flow over an elongated sheet with Darcy-Forchheimer medium. Proc Inst Mech Eng Part E J Process Mech Eng. 2025;239:821–9.
37. Hussein UN, Khashi'ie NS, Arifin NM, Pop I. Heat Transfer and Flow Dynamics of Ternary Hybrid Nanofluid over a Permeable Disk under Magnetic Field and Joule Heating Effects. Front Heat Mass Transf. 2025;23:383–95.
38. Naveed M, Ali S, Hasnain J, Abbas Z. Analysis of the effect of joule heating and hall current on flow of hybrid nanofluid over a curved stretching surface with melting boundary condition. Heat Transf Res 2021; 52
39. Patel VK, Pandya JU, Patel MR. Thermal and velocity slip conditions together with thermal radiative effects on Joule heating mixed convection MHD hybrid nanofluid flow induced by an exponentially shrinking or stretching sheet. Int J Model Simul 2024; 1–27
40. Mumtaz F, Al-Zubaidi A, Abbas T, Saleem S. Thermal performance analysis of quaternary hybrid nanofluids with radiative and Joule heating effects in magnetohydrodynamic flow over a stretched surface. Results Phys. 2025;71:108176.
41. Ramesh K, Warke AS, Kotecha K, Vajravelu K. Numerical and artificial neural network modelling of magnetorheological radiative hybrid nanofluid flow with Joule heating effects. J Magn Magn Mater. 2023;570:170552.
42. Yasir M, Khan M. Thermal efficiencies of Ohmic cobalt ferrite and magnetite hybrid ferrofluid flow over an exponentially vertically shrinking surface. Alex Eng J. 2024;90:120–8.
43. Rasheed HU, Islam S, Zeeshan, Abbas T, Khan J. Analytical treatment of MHD flow and chemically reactive Casson fluid with Joule heating and variable viscosity effect. Waves Random Complex Media 2022; 1–17
44. Riaz S, Afzaal MF, Wang Z, Jan A, Farooq U. Numerical heat transfer of non-similar ternary hybrid nanofluid flow over linearly stretching surface. Numer Heat Transf Part A Appl. 2024;85:4021–35.

45. Waqas H, Farooq U, Liu D, Abid M, Imran M, Muhammad T. Heat transfer analysis of hybrid nanofluid flow with thermal radiation through a stretching sheet: a comparative study. Int Commun Heat Mass Transf. 2022;138:106303. https://doi.org/10.1016/J.ICHEATMASSTRANSFER.2022.106303.
46. Ziabakhsh Z, Domairry G, Bararnia H, Babazadeh H. Analytical solution of flow and diffusion of chemically reactive species over a nonlinearly stretching sheet immersed in a porous medium. J Taiwan Inst Chem Eng. 2010;41:22–8.
47. Kausar MS, Waqas M, Shehzad SA, Hosseinzadeh K, Hejazi HA, Mtaouaa W. Numerical computations for Darcy–Forchheimer-based dual convection reactive flow considering Casson nanomaterial by convected permeable surface. Int J Mod Phys B 2024; 2450426.
48. Zangooee MR, Hosseinzadeh K, Ganj DD. Investigation of three-dimensional hybrid nanofluid flow affected by nonuniform MHD over exponential stretching/shrinking plate. Nonlinear Eng. 2022;11:143–55.
49. Abas SA, Ullah H, Islam S, Fiza M. A passive control of magnetohydrodynamic flow of a blood-based Casson hybrid nanofluid over a convectively heated bi-directional stretching surface. ZAMM J Appl Math Mech Für Angew Math Und Mech. 2024;104:e202200576.
50. Zainal NA, Nazar R, Naganthran K, Pop I. Viscous dissipation and MHD hybrid nanofluid flow towards an exponentially stretching/shrinking surface. Neural Comput Appl 2021; 1–11
51. Ahmad F, Abdal S, Ayed H, Hussain S, Salim S, Almatroud AO. The improved thermal efficiency of Maxwell hybrid nanofluid comprising of graphene oxide plus silver/kerosene oil over stretching sheet. Case Stud Therm Eng. 2021;27:101257.
52. Zainal NA, Nazar R, Naganthran K, Pop I. The impact of thermal radiation on Maxwell hybrid nanofluids in the stagnation region. Nanomaterials. 2022;12:1109.
53. Birkea FMO, Abas SA, Ullah H, Fiza M, Jan AU, Elaissi S, et al. Significance of nanoparticle diameter and inter-particle spacing in the oblique stagnation point flow over a convectively heated cylinder. J Radiat Res Appl Sci. 2025;18:101674.
54. Dawar A, Islam S, Shah Z, Mahmuod SR, Lone SA. Dynamics of inter-particle spacing, nanoparticle radius, inclined magnetic field and nonlinear thermal radiation on the water-based copper nanofluid flow past a convectively heated stretching surface with mass flux condition: A strong suction case. Int Commun Heat Mass Transf. 2022;137:106286.
55. Anwar T, Abas SA, Fiza M, Ullah H, Al-Melhafi SM. Viscous Dissipative Ternary Nanoparticles on Heat Transfer Enhancement in MHD Flow Over a Stretching Surface. Int J Thermofluids 2025; 101327
56. Yasmin H, Bossly R, Alduais FS, Al-Bossly A, Saeed A. Thermally radiative water-based hybrid nanofluid with nanoparticles and gyrotactic microorganisms past a stretching surface with convective conditions and porous media. Case Stud Therm Eng. 2025;65:105644.
57. Hamad MAA. Analytical solution of natural convection flow of a nanofluid over a linearly stretching sheet in the presence of magnetic field. Int Commun Heat Mass Transf. 2011;38:487–92.

Publisher's Note

Springer Nature remains neutral with regard to jurisdictional claims in published maps and institutional affiliations.